Journal of Power Sources 642 (2025) 237011

Contents lists available at ScienceDirect

Journal of Power Sources

journal homepage: www.elsevier.com/locate/jpowsour

# Lithium nitrate reservoir enabling substantial improvement in the cycle life of anode-free and lithium metal batteries

Myung-Keun Oh [a], Ji-Wan Kim [a], Hee-Su Kim [a], Dong-Won Kim [a,b,*]

[a] Department of Chemical Engineering, Hanyang University, Seoul, 04763, Republic of Korea
[b] Department of Battery Engineering, Hanyang University, Seoul, 04763, Republic of Korea

## HIGHLIGHTS

- $LiNO_3$ reservoir (LNR) stored and continuously released $LiNO_3$ into the electrolyte.
- The LNR enabled the formation and maintenance of a stable SEI layer on the Li anode.
- The lithium metal battery with LNR exhibited superior cycling performance.

## GRAPHICAL ABSTRACT

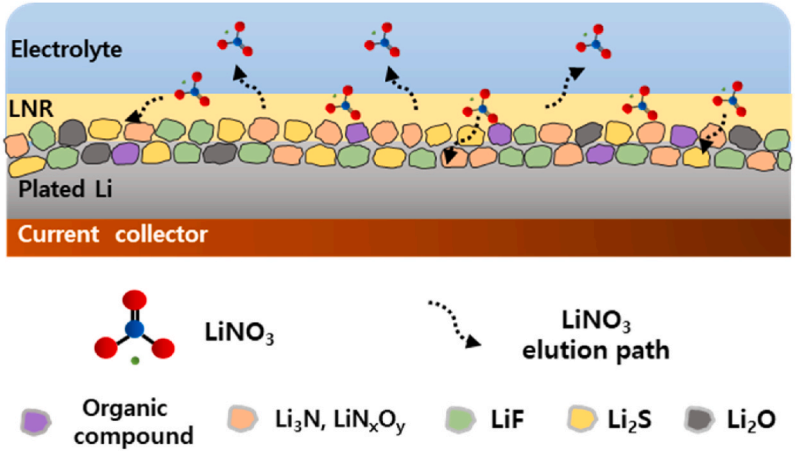


## ARTICLE INFO

*Keywords:*
Lithium nitrate
Lithium metal battery
Anode-free battery
Solid electrolyte interphase
Lithium dendrite

## ABSTRACT

Li metal batteries attract significant attention owing to their high energy densities; however, the growth of Li dendrites and high reactivities of Li metal with liquid electrolytes lead to performance degradation and safety problems. As a solid electrolyte interphase (SEI)-forming additive for use in addressing these problems, $LiNO_3$ stabilizes lithium metal by forming a robust, stable SEI on the Li anode surface. However, the use of $LiNO_3$ is limited owing to its low degree of dissociation within the electrolyte. In this study, we propose a $LiNO_3$ reservoir (LNR) that can store and continuously release $LiNO_3$ into the electrolyte during charge-discharge cycling, which enables the formation and maintenance of a stable SEI layer on the lithium metal anode. Due to uniform Li deposition/stripping and the suppression of dendritic Li growth in the presence of the LNR, the anode-free and lithium (20 μm)/$LiNi_{0.8}Co_{0.1}Mn_{0.1}O_2$ cells with the LNR exhibit superior cycling performance compared to those of the cells without the LNR. The detailed mechanism of the substantial improvement in the cycling performance using the LNR is investigated using X-ray photoelectron spectroscopy, NMR spectroscopy, electrochemical impedance spectroscopy, and scanning electron microscopy.

* Corresponding author. Department of Chemical Engineering, Hanyang University, Seoul, 04763, Republic of Korea.
*E-mail address:* dongwonkim@hanyang.ac.kr (D.-W. Kim).

https://doi.org/10.1016/j.jpowsour.2025.237011
Received 27 November 2024; Received in revised form 20 March 2025; Accepted 7 April 2025
Available online 12 April 2025

## 1. Introduction

The demand for rechargeable lithium batteries with high energy densities has increased with the expansion of the green electric vehicle market [1,2]. Lithium metal is a promising anode material used for fabricating lithium batteries with high energy densities owing to its high specific capacity and low redox potential [3–5]. Anode-free batteries with higher energy densities can be prepared without using lithium metal, and they exhibit numerous advantages, such as simplified fabrication processes, reduced costs, and enhanced safety compared to lithium metal batteries [6,7]. However, lithium metal undergoes undesirable side reactions with the liquid electrolyte, forming a resistive, unstable solid electrolyte interphase (SEI) during cycling. Moreover, lithium dendrites that cause internal short circuits grow at the anode surface owing to non-uniform Li deposition and stripping during repeated charging/discharging, and dead (inactive) lithium can be formed, which leads to significant capacity loss during battery operation [8,9]. To address these problems, SEI-forming additives, such as fluoroethylene carbonate, vinylene carbonate, $LiNO_3$, lithium difluoro (oxalato)borate, and $LiBF_4$, were incorporated into liquid electrolytes to suppress dendritic Li growth and form stable SEI layers on lithium metal anodes [10–15]. $LiNO_3$ exhibits a synergistic effect when applied as an additive with lithium bis(fluorosulfonyl)imide (LiFSI) by forming Li-N compounds with high ionic conductivities and LiF with excellent mechanical properties at the surface of Li anode. This is because the addition of $LiNO_3$ in the electrolyte resulted in a change of solvation structure where $FSI^-$ anions exhibited closer distance to $Li^+$ ions, resulting the promotion of the reductive decomposition of $FSI^-$ anions on the Li anode [16]. These SEI components (Li-N and LiF) effectively inhibit the formation and growth of Li dendrites [17]; however, the complete dissolution of $LiNO_3$ in liquid electrolytes is still challenging [18]. To overcome the low degree of $LiNO_3$ dissociation, various studies regarding the storage and elution of $LiNO_3$ using separators, Li-metal powder electrodes, and porous polymer substrates have been reported [19–21]. The continuously released $LiNO_3$ can reconstruct and stabilize the SEI layer, thus enhancing the cycle life of the Li metal battery. However, these strategies can clog the pores of the porous substrate or reduce the energy density of the Li metal battery for practical applications.

In this study, we propose a $LiNO_3$ reservoir (LNR) using a thin, fibrous poly (vinylidene fluoride-*co*-hexafluoropropylene) (PVdF-*co*-HFP) membrane as a framework. We used PVdF-*co*-HFP as the framework for the $LiNO_3$ reservoir, because it could be processed to thin and porous membrane by electrospinning method. Furthermore, it is electrochemically stable within the operation voltage of the lithium metal batteries and has good compatibility with liquid electrolyte [22]. The highly porous electrospun membrane facilitated the storage and continuous release of $LiNO_3$ during the charge/discharge cycling. The anode-free and Li metal batteries with the LNR and high mass-loaded $LiNi_{0.8}Co_{0.1}Mn_{0.1}O_2$ (NCM) cathode (active mass loading: 19.4 mg $cm^{-2}$) exhibited high levels of capacity retention of 68.8 % after 100 cycles and 85.0 % after 300 cycles, respectively, at 0.33 C rate and 25 °C. The enhancement in the cycling performance of the cells with the LNR were analyzed using various techniques, such as X-ray photoelectron spectroscopy (XPS), $^6$Li solid and $^7$Li solution nuclear magnetic resonance (NMR) spectroscopy, electrochemical impedance spectroscopy (EIS), and scanning electron microscopy (SEM).

## 2. Material and methods

### 2.1. Materials

$LiNO_3$ (Sigma-Aldrich), LiCl (Sigma-Aldrich), and PVdF-*co*-HFP (molecular weight: 470 000 g $mol^{-1}$, Kynar Flex 2801, Arkema) were used after vacuum drying at 90 °C for 12 h. The liquid electrolyte, which was supplied by Enchem, was 2.5 M LiFSI dissolved in a 4:1 (v/v) mixture of 1,2-dimethoxyethane (DME) and 1,1,2,2-tetrafluoroethyl 2,2,2-trifluoroethyl ether (TFOFE), with 1 wt% $LiNO_3$ as an additive. DME was chosen as the primary solvent due to its superior stability toward Li metal compared to carbonate solvents, and TFOFE was incorporated as a diluent to reduce the viscosity of the electrolyte, resulting in forming a localized high-concentration electrolyte [23,24]. The maximum concentration of $LiNO_3$ that could be dissolved in the electrolyte was 1.0 wt% (0.17 M). The viscosity and ionic conductivity of the electrolyte were 10.8 cP and 6.1 x $10^{-3}$ S $cm^{-1}$ at 25 °C, respectively. A polyethylene (PE) separator (thickness: 16 μm, SKIET) was vacuum-dried at 90 °C for 12 h prior to use, and Li metal (thickness: 20 μm, Honjo Metal) was used as an anode after pressing it onto a copper current collector (thickness: 10 μm).

### 2.2. Preparation of the LNR

A porous polymer membrane was fabricated via electrospinning of a polymer solution. The solution was prepared by dissolving 16 wt% PVdF-*co*-HFP in acetone/*N,N*-dimethylacetamide (7/3, v/v), followed by heating at 60 °C for 3 h. The resulting solution was electrospun onto an aluminum foil at 6 kV and 4.0 mL $min^{-1}$, and the obtained membrane was then dried in a vacuum oven at 80 °C for 12 h. The porosity of the membrane was approximately 70 %. An impregnation solution was prepared by dissolving 0.8 M $LiNO_3$ in ethanol. After soaking the electrospun membrane in the solution for 5 min, it was vacuum-dried at 100 °C for 12 h, and the obtained LNR film displayed a thickness of 5.5 μm. The amount of $LiNO_3$ in the LNR was about 1.47 g $cm^{-3}$, indicating $LiNO_3$ filled 61.7 % of the total pores in the electrospun membrane.

### 2.3. Cell assembly and electrochemical studies

The LNR was pressed onto a Cu (for an anode-free cell) or Li anode (for a Li metal cell). The cell was assembled by stacking the LNR on the Cu/Li anode, PE separator, and NCM cathode in a CR2032-type coin cell. The active-material content in the cathode on Al foil (foil thickness: 10 μm) was 96.0 wt%, and its loading was approximately 19.4 mg $cm^{-2}$. The density of cathode was 3.52 g $cm^{-3}$. The liquid electrolyte (electrolyte-to-capacity ratio: 4.5 g $Ah^{-1}$) was then injected into the cell. The cells were assembled in a high-purity argon-filled glove box (MBRAUN). EIS was performed to measure the interfacial resistance of the cell during cycling in the frequency range 0.1–1 000 000 Hz using an impedance analyzer (ZIVE MP1, WonATech). Linear sweep voltammetry (LSV) was conducted at a scan rate of 0.1 mV $s^{-1}$ using a CHI660 analyzer (CH Instruments). Galvanostatic cycling studies of the anode-free and Li/NCM cells were performed in the potential range 3.0–4.2 V at 25 °C using a battery tester (WBCS3000, WonATech). During the preconditioning cycle, the cell was charged and discharged at 0.1 C rate for two cycles. After preconditioning, the cell was charged and discharged at 0.33 C rate and 25 °C.

### 2.4. Characterization

Solid-state $^6$Li NMR spectroscopy of the SEI components collected from the anode was performed using a 500 MHz Avance III HD solid-state NMR spectrometer (Bruker). The morphology of the Li anode was examined using field-emission SEM (Verios G4 UC, FEI), and the chemical composition of the surface layer on the electrode was investigated using XPS (K-Alpha$^+$, Thermo Fisher Scientific). $^7$Li NMR spectra were obtained by VNMRS 600 MHz spectrometer (Agilent Technologies), and DME (99.9 %, Sigma-Aldrich) and 3 M LiCl in $D_2O$ (99.9 %, Sigma-Aldrich) were used as the solvent and reference, respectively.

## 3. Results and discussion

The electrospun PVdF-*co*-HFP membrane without soaking in $LiNO_3$-containing solution has many pores that are not filled with $LiNO_3$, as

presented in Fig. S1a. We obtained the pore size distribution of the electrospun membrane by using ImageJ software, as depicted in Fig. S1b, showing that a pore size is in the range of 2~10 μm with an average size of 5.2 μm. The presence of $LiNO_3$ in the LNR layer was confirmed by the SEM and energy-dispersive X-ray spectroscopy (EDS) mapping images, as shown in Fig. 1a and b. The C and F elements, arising from PVDF-*co*-HFP, are observed within the electrospun fibers. In addition, the N and O elements within $LiNO_3$ can be observed in the pores of the electrospun membrane, indicating that the $LiNO_3$ additive fills the pores. The mechanical properties of PE, PVdF-co-HFP membrane and LNR were measured using a nano indenter, and the results are summarized in Table S1. While the LNR prepared with PVdF-co-HFP membrane exhibits lower mechanical properties compared to PE separator, its superior recovery characteristics enable it to effectively accommodate deformation caused by volume changes of lithium during repeated charge and discharge cycles. We measured the ionic and electronic conductivities of the PVdF-co-HFP membrane and LNR. To maintain the same conditions as the Li/NCM cell, the ionic conductivity was measured after soaking them with PE separator in liquid electrolyte. As a result, the LNR exhibited an ionic conductivity of $4.4 \times 10^{-4}$ S $cm^{-1}$, which was lower than that of the PVdF-co-HFP membrane ($5.5 \times 10^{-4}$ S $cm^{-1}$). The reduction in ionic conductivity can be attributed to the filling of $LiNO_3$ in the pores of the electrospun membrane, which hinders ion transport. With respect to electronic conductivity, the electronic conductivity of LNR was too low (less than $10^{-16}$ S $cm^{-1}$) to be measured. To confirm the electrochemical reduction of the $LiNO_3$ within the LNR, linear sweep voltammetry was performed using 2.5 M LiFSI in DME/TFOFE ($LiNO_3$-free electrolyte) with and without the LNR. As shown in Fig. 1c, an additional cathodic peak is observed at 1.62 V vs. $Li/Li^+$ in the presence of the LNR. This peak can be attributed to the reduction of $LiNO_3$ released from the LNR [25,26], as it is not observed in the voltammogram of the cell without the LNR. This suggests that $LiNO_3$ released from the LNR was reduced at a low potential prior to the electrodeposition of Li on the electrode. From the cyclic voltammogram (CV) with LNR (Fig. S2a), we could observe only the reductive peak of $LiNO_3$ without the oxidative peak of its reduction product, indicating that $LiNO_3$ is irreversibly reduced. We also compared CVs of the cells with $LiNO_3$ added directly to the electrolyte and with the $LiNO_3$ reservoir (LNR). As presented in Fig. S2b, the two CVs exhibited almost the same electrochemical behavior.

To confirm the release of $LiNO_3$ from the LNR and its involvement in the formation of the SEI on the anode during cycling, the anode-free NCM cells with and without the LNR were assembled and subjected to 10 charge/discharge cycles at 0.33 C and 25 °C. The configuration of the anode-free NCM cell with the LNR on a Cu current collector is shown in Fig. S3. To investigate the effect of the $LiNO_3$ within the LNR on SEI formation, the electrolyte used to assemble the cells was $LiNO_3$-free 2.5 M LiFSI in DME/TFOFE (4/1, v/v). Fig. S4 shows the XPS spectra of the Li plated on the Cu foil at the charged state after 10 cycles. Clearly, the SEI formed on the plated Li displays different chemical components, depending on the presence of the LNR. When the LNR is employed, additional components, such as $Li_3N$ and $LiN_xO_y$, are observed, along with an increase in the intensity of the LiF component. These results suggest that $LiNO_3$ embedded within the LNR is released into the electrolyte, and it is involved in the formation of the SEI on the anode surface during the repeated cycling [27,28]. The SEI components formed on the anode were examined using solid-state $^6Li$ NMR isotope analysis. For use in $^6Li$ NMR isotope analysis, $^6LiNO_3$ was synthesized by reacting $^6Li$ metal and an aqueous $HNO_3$ solution ($2\ ^6Li + 2\ HNO_3 \leftrightarrow 2\ ^6LiNO_3 + H_2$) under an argon atmosphere. It is noticeable that the isotope ratio of $^6Li$

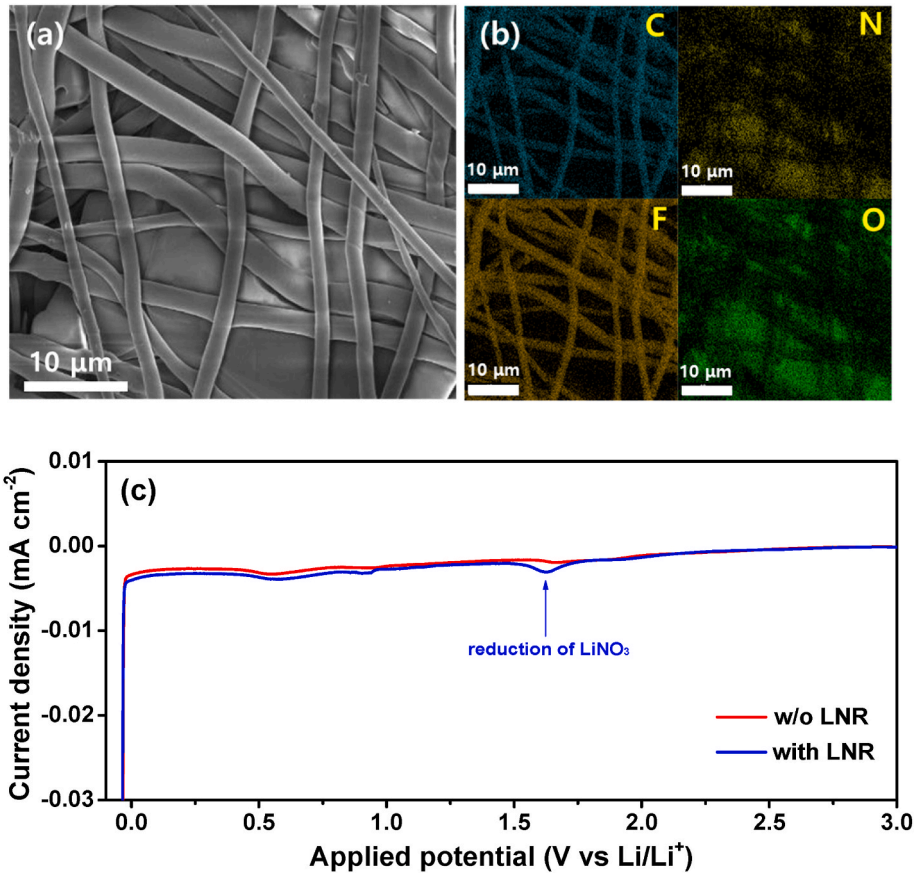


**Fig. 1.** (a) Surface SEM image of the LNR and (b) its EDS mapping images. (c) Linear sweep voltammograms of the Li/stainless steel cells employing 2.5 M LiFSI in DME/TFOFE ($LiNO_3$-free electrolyte) with and without the LNR.

and $^{7}Li$ is 7.5 : 92.5 by atomic %. Fig. S5 shows the solid-state $^{6}Li$ NMR spectra of the synthesized $^{6}LiNO_3$ and commercial $LiNO_3$ (mixture of $^{7}LiNO_3$ and $^{6}LiNO_3$, with $^{7}LiNO_3$ as the main component), confirming that $^{6}LiNO_3$ is successfully synthesized using $^{6}Li$ metal and $HNO_3$. The LNRs were prepared using electrospun PVDF-*co*-HFP and $^{6}LiNO_3$ instead of commercial $LiNO_3$ and applied to anode-free NCM cells. After 10 charge−discharge cycles, the SEI layer formed on the anode was sampled at the discharged state under an inert argon atmosphere and subjected to solid-state $^{6}Li$ NMR spectroscopy. As shown in Fig. S6, the obtained spectrum can be resolved into numerous peaks, corresponding to $^{6}Li_3N$ (7.4 ppm), $^{6}Li_2O$ (2.8 ppm), $^{6}Li_2S$ (2.4 ppm), $^{6}LiOH$ (1.3 ppm), $^{6}LiF$ (−0.9 ppm), and $CH_3O^{6}Li$ (−0.1 ppm) [29–31]. Therefore, the $^{6}LiNO_3$ within the LNR is released into the electrolyte and is participated in the formation of the SEI on the anode during the cycling of the anode-free cell.

Anode-free NCM cells with and without the LNR were assembled using the $LiNO_3$-containing electrolyte (2.5 M LiFSI in DME/TFOFE with 1 wt% $LiNO_3$), and their cycling performance was evaluated. Fig. 2a and b, respectively, show the cycling profiles of the anode-free cells without and with the LNR at 0.33 C rate and 25 °C. The two cells initially deliver almost identical discharge capacities, irrespective of the presence of the LNR. However, the cell without the LNR exhibits rapid capacity fading with subsequent cycling, finally leading to cell failure after 50 cycles. In contrast, the anode-free cell with the LNR exhibits stable cycling behavior despite the use of a highly mass-loaded NCM cathode, maintaining a capacity retention of 68.8 % after 100 cycles. The coulombic

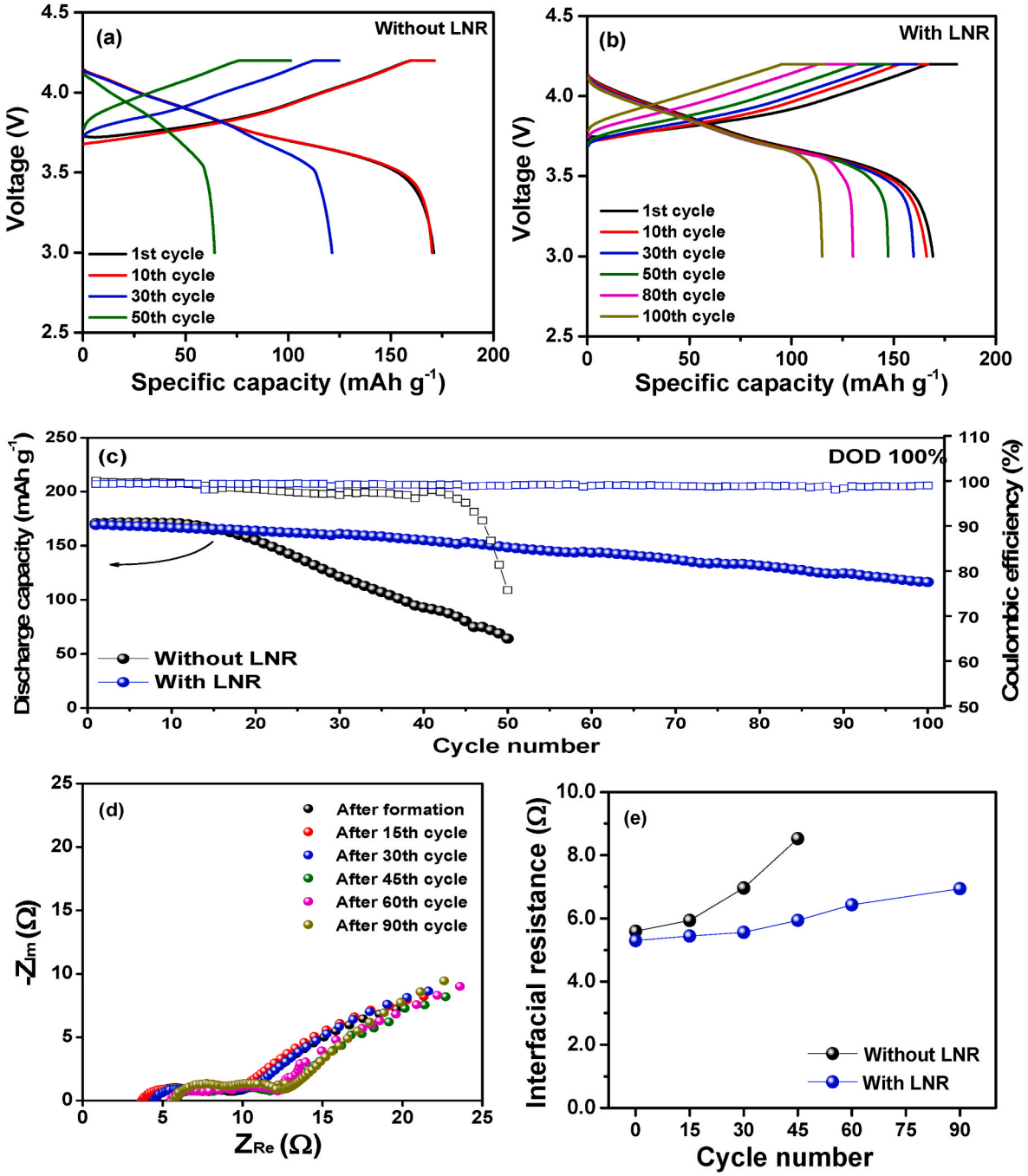


**Fig. 2.** Voltage profiles of the anode-free NCM cells (a) without and (b) with the LNR at 0.33 C. (c) Cycling performance of the anode-free NCM cells at 0.33 C and 25 °C. (d) AC impedance spectra of the anode-free NCM cell with the LNR and (e) variations in the interfacial resistances of the anode-free NCM cells with cycling.

efficiency of the cell with the LNR exceeds that of the cell without the LNR throughout cycling, as shown in Fig. 2c. The alternating-current (AC) impedances of the cells were measured during cycling, and the impedance spectra of the cell with the LNR are shown in Fig. 2d, displaying two overlapping semicircles. The first semicircle, which is observed in the high-frequency region, is related to the ionic resistance of the film formed on the electrode surface ($R_f$). The second semicircle, which is observed in the low-frequency region, is attributed to the charge transfer resistance at the interface ($R_{ct}$) [32,33]. Accordingly, the overall interfacial resistance of the cell ($R_{int}$) can be regarded as the sum of $R_f$ and $R_{ct}$. The variations in the $R_{int}$ values of the two different cells with cycling are shown in Fig. 2e. In earlier (<15) cycles, the two cells exhibit similar $R_{int}$ values. After the 15th cycle, at which the capacity of the cell without the LNR rapidly decreases, the $R_{int}$ of this cell significantly increases, whereas the $R_{int}$ of the cell with the LNR only increases slightly. These results suggest that the LNR is critical in maintaining a stable $R_{int}$, which can be ascribed to the continuous release of $LiNO_3$ and its involvement in the formation of a stable SEI layer.

Fig. 3 shows the surface and cross-sectional SEM images of the plated Li anodes on Cu foils at their charged states, as obtained after the first preconditioning and 50th cycles of the anode-free NCM cells. Please note that SEM analysis was conducted after removing the LNR from the Li anode. In the cell without the LNR, the plated Li exhibits a dense morphology, with a thickness of 25.2 μm, after the first preconditioning cycle (Fig. 3a and b). However, after 50 cycles, the deposited Li exhibits a rough, porous morphology, with numerous cracks on the surface (Fig. 3c and its enlarged image), and the thickness remarkably increases from 25.2 to 68.5 μm (Fig. 3d). In contrast, the plated Li anode in the cell with the LNR displays compact, uniform surface morphologies after the first preconditioning and 50th cycles (Fig. 3e and g). In the enlarged surface image of deposited Li after 50 cycles, it shows relatively larger and non-dendritic surface morphology. The thickness of the deposited Li, excluding that of the LNR layer (5.5 μm), is increased from 23.8 to 37.0 μm after 50 cycles (Fig. 3f and h). We measured the grain size of plated lithium, and the results are presented in Fig. S7. Without LNR, the average grain size of lithium was approximately 0.84 μm. On the other hand, when LNR is applied onto the Cu foil, the average grain size was increased to 4.9 μm, indicating the presence of LNR enabled the more uniform deposition of lithium on the Cu foil. These results suggest that the presence of the LNR suppresses the growth of Li dendrites and promotes the compact deposition of Li. This is due to the formation of a stable, robust SEI layer on the plated Li owing to the continuous release of $LiNO_3$ from the LNR [34]. We obtained the cross-sectional EDS mapping image of the Li anode with LNR after 50 cycles (Fig. S8). It reveals that nitrogen elements are uniformly distributed in the SEI layer on the plated Li. The nitrogen atoms in the SEI layer arises from nitrogen compounds such as $Li_3N$ and $LiN_xO_y$.

To monitor the chemical composition of the SEI layer during cycling, XPS of the plated Li in the cell with LNR was conducted after the 10th and 50th cycles, and the results are shown in Fig. 4. The C 1s spectrum is normalized relative to the intensity of the C–C peak associated with conductive carbon [35,36]. After 10 cycles, the C 1s XPS spectrum displays peaks corresponding to O–C–H/C–C (284.9 eV), C–O–C (286.5 eV), and C–F (289.3 eV). The O–C–H/C–C and C–O–C peaks may be attributed to $CH_3OLi$ and organic-based compounds arising from the decomposition of DME and TFOFE solvents [37]. After 50 cycles, the XPS spectrum of the plated Li displays the same C 1s peaks with lower intensities, indicating that the decomposition of the organic solvents is suppressed in later cycles. The peak intensities in the N 1s XPS spectra are normalized relative to that of $LiNO_3$ at 407.5 eV. After the 10th and 50th cycles, the N 1s XPS spectrum displays the same peaks, corresponding to N–S (399.8 eV), $Li_3N$ (398.5 eV), and $LiN_xO_y$ (396.9 eV), with almost identical intensities, due to the reductive decomposition of LiFSI and $LiNO_3$ [16,38]. It should be noted that the $LiNO_3$ content after 50 cycles was lower than that after 10 cycles. The decrease of $LiNO_3$ content with cycling can be interpreted as a result of continuous release of $LiNO_3$ into the electrolyte, where it is reduced on the anode surface. The peak intensities in the F 1s spectra are normalized relative to those of C–F (PVdF-*co*-HFP) at 687.8 eV. After 50 cycles, the LiF peak at 684.9 eV increases in intensity. Notably, LiF can be produced within the SEI layer via the reductive decomposition of LiFSI in the presence of $LiNO_3$ [16]. Accordingly, these results suggest that $LiNO_3$ is continuously released from the LNR into the liquid electrolyte and acts as an SEI-forming additive during cycling. For comparison, the XPS spectra of the plated Li in the cell without the LNR after 10 and 50 cycles were analyzed, as shown in Fig. S9. After 10 cycles, the SEI layer on the plated

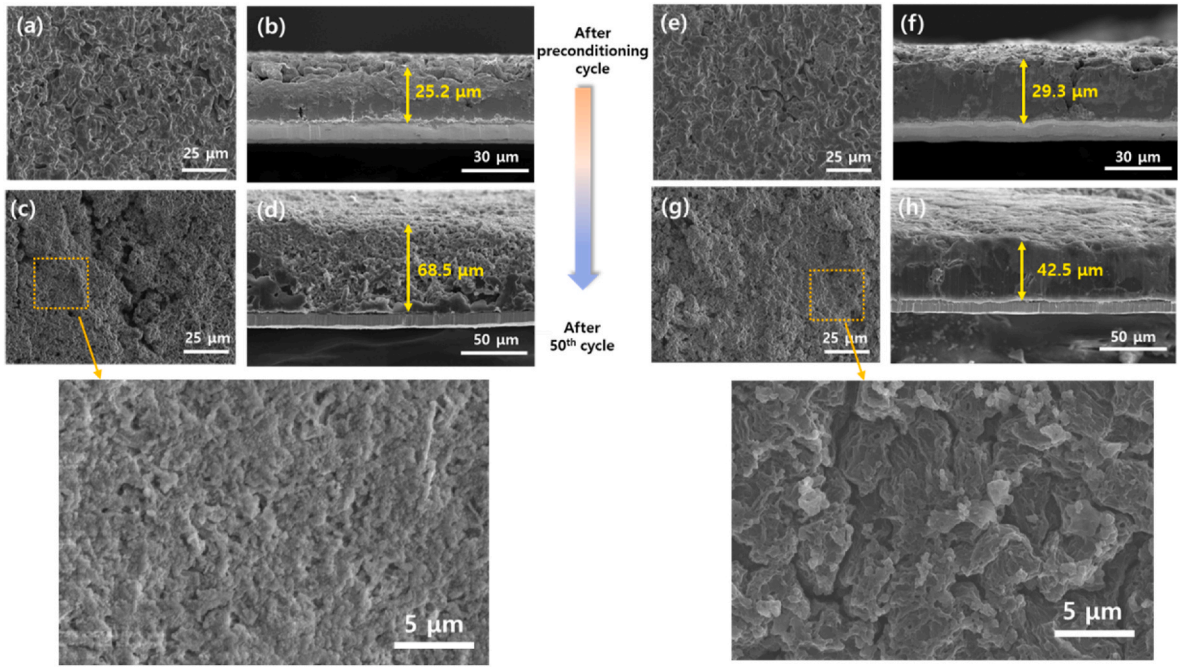


**Fig. 3.** (a, c) Surface and (b, d) cross-sectional SEM images of the plated Li on Cu foil without the LNR in the charged state. (e, g) Surface and (f, h) cross-sectional SEM images of the plated Li on Cu foil with the LNR in the charged state. SEM was performed after the first preconditioning and 50th cycles.

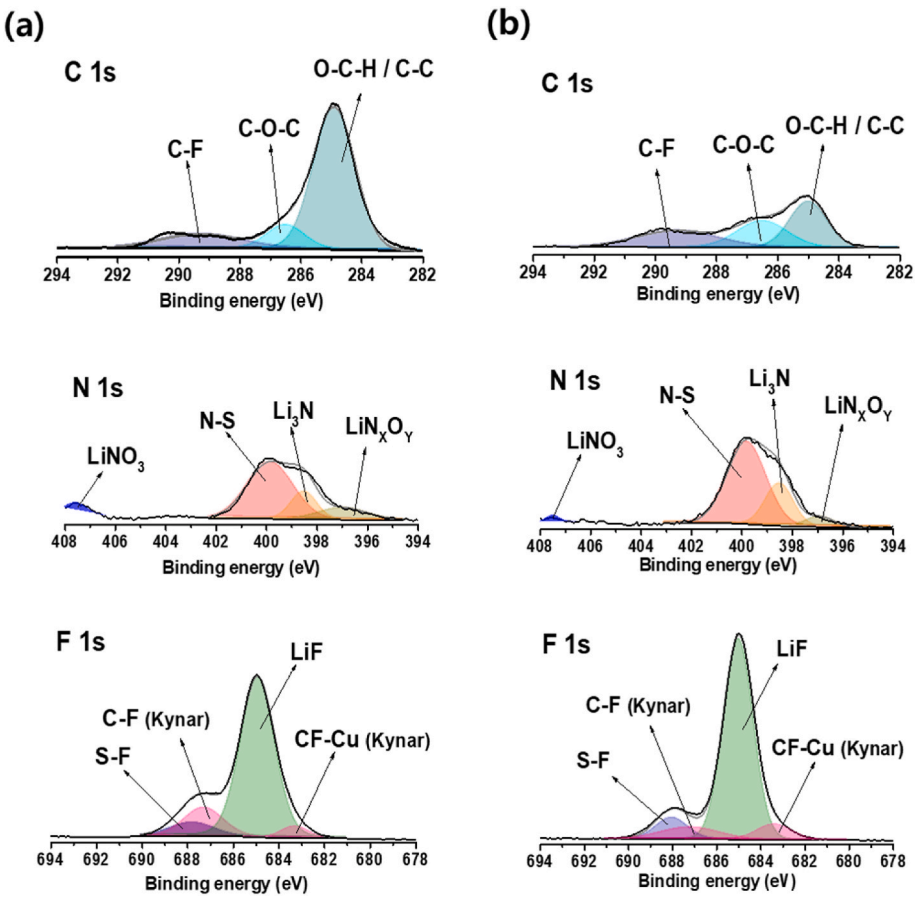


**Fig. 4.** C 1s, N 1s, and F 1s XPS spectra of the plated Li electrode with the LNR in the charged state after the (a) 10th and (b) 50th cycles.

Li exhibits O–C–H/C–C, $Li_3N$, $LiN_xO_y$, and LiF with high intensities, which are well-known SEI components formed in the electrolyte in the presence of LiFSI and $LiNO_3$. Remarkably, the $LiN_xO_y$ component of the SEI is hardly observed after 50 cycles, and the peak intensity of LiF is significantly decreased. In addition, the organic components (C–O–C, O–C–H/C–C) produced via the decomposition of DME and TFOFE are retained after 50 cycles, as shown in the C 1s spectrum. Hence, the $LiNO_3$ dissolved in the electrolyte is completely consumed as an SEI-forming additive during the initial cycles and is not involved in SEI formation in the later cycles.

Based on these results, SEI formation on the plated Li with and without the LNR is schematically illustrated in Fig. 5. During the earlier cycles, the SEI layers formed on Li exhibit almost identical compositions, irrespective of the presence of the LNR, because the electrolytes in both cells initially contain small amounts of $LiNO_3$. However, its concentration gradually decreases with cycling in the cell without the LNR, because it is involved in SEI formation and completely depleted in the electrolyte in the later cycles. In contrast, in the cell with the LNR, the continuous release of $LiNO_3$ from the LNR delays its depletion within the electrolyte. Accordingly, an SEI layer comprising LiF with a high mechanical strength and $Li_3N/LiN_xO_y$ with a high $Li^+$ conductivity, is maintained during the Li deposition/stripping cycles [39–42]. The

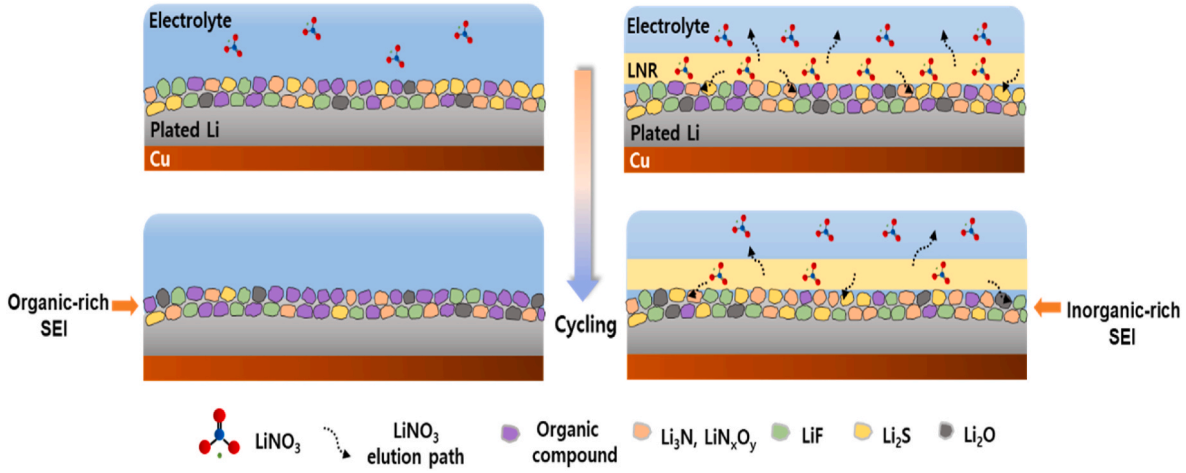


**Fig. 5.** Schematic illustration of SEI formation on the plated Li when using (a) Cu or (b) LNR@Cu in the anode-free NCM cell with repeated cycling.

inorganic-rich and mechanically robust SEI layer suppresses dendritic Li growth and the deleterious reactions of the electrolyte during cycling, leading to the enhanced cycling stability of the anode-free cell, as shown in Fig. 2c.

We quantitatively analyzed the $LiNO_3$ release behavior of the cells during cycling using $^7$Li NMR spectroscopy [43,44]. To investigate the effect of the $LiNO_3$ concentration on the chemical shift, the $^7$Li NMR spectra of liquid electrolytes containing different concentrations of $LiNO_3$ (0–0.58 M) were measured, as shown in Fig. S10a. The peak shifts downfield with increasing $LiNO_3$ concentration owing to the increase in the donor number caused by $LiNO_3$ addition to the electrolyte [45]. Based on these results, a correlation curve between the $LiNO_3$ concentration and chemical shift of the $^7$Li NMR peak can be constructed, as shown in Fig. S10b. The variation in the chemical shift with LiFSI concentration was also examined while maintaining the concentration of $LiNO_3$ within the electrolyte. As shown in Fig. S11, little change is observed in the chemical shift of the $^7$Li peak when the $LiNO_3$ concentration remains constant. Therefore, the NMR chemical shift is primarily governed by the amount of $LiNO_3$ within the electrolyte, which enables the quantitative analysis of the $LiNO_3$ content within the cell during cycling. Fig. 6a shows the $^7$Li NMR spectrum of the electrolyte collected from the anode-free cell without the LNR as a function of the cycle number. It should be noted that the $LiNO_3$ concentration in Fig. 6 was measured in the cell (including anode, LNR, separator, and cathode), because the amount of liquid electrolyte sampled from the cell was too small after extended cycles. The NMR peak shifts up-field as cycling progresses, indicating a gradual decrease in the $LiNO_3$ content with cycling. The $LiNO_3$ concentration was calculated based on the correlation curve of the chemical shift as a function of the $LiNO_3$ concentration, as shown in Fig. S10b, and the results are shown in Fig. 6b. The $LiNO_3$ concentration decreases remarkably from 0.16 to 0.07 M after the first preconditioning cycle, indicating that a significant amount of $LiNO_3$ is consumed in forming the SEI during this cycle. The $LiNO_3$ concentration gradually decreases with subsequent cycling, and no $LiNO_3$ is observed after 50 cycles. Similarly, the $LiNO_3$ concentration was also measured in the electrolyte collected from the Li/NCM cell with LNR. The corresponding $^7$Li NMR spectra and variation in the $LiNO_3$ concentration with cycling are shown in Fig. 6c and d, respectively. The $LiNO_3$ consumption pattern in the cell with LNR exhibits a trend similar to that of the cell without the LNR. However, the main difference between the two cells is that the $LiNO_3$ concentration is even maintained at 0.12 M after 100 cycles in the cell with the LNR. These results suggest that $LiNO_3$ is continuously consumed because of its involvement in SEI formation and is released from the LNR into the electrolyte during cycling. Therefore, the enhanced cycling stability of the cell with the LNR may be attributed to the formation of a stable, robust inorganic-rich SEI owing to the continuous release of $LiNO_3$ from the LNR.

The LNR was also applied to the Li metal cell to improve its cycling

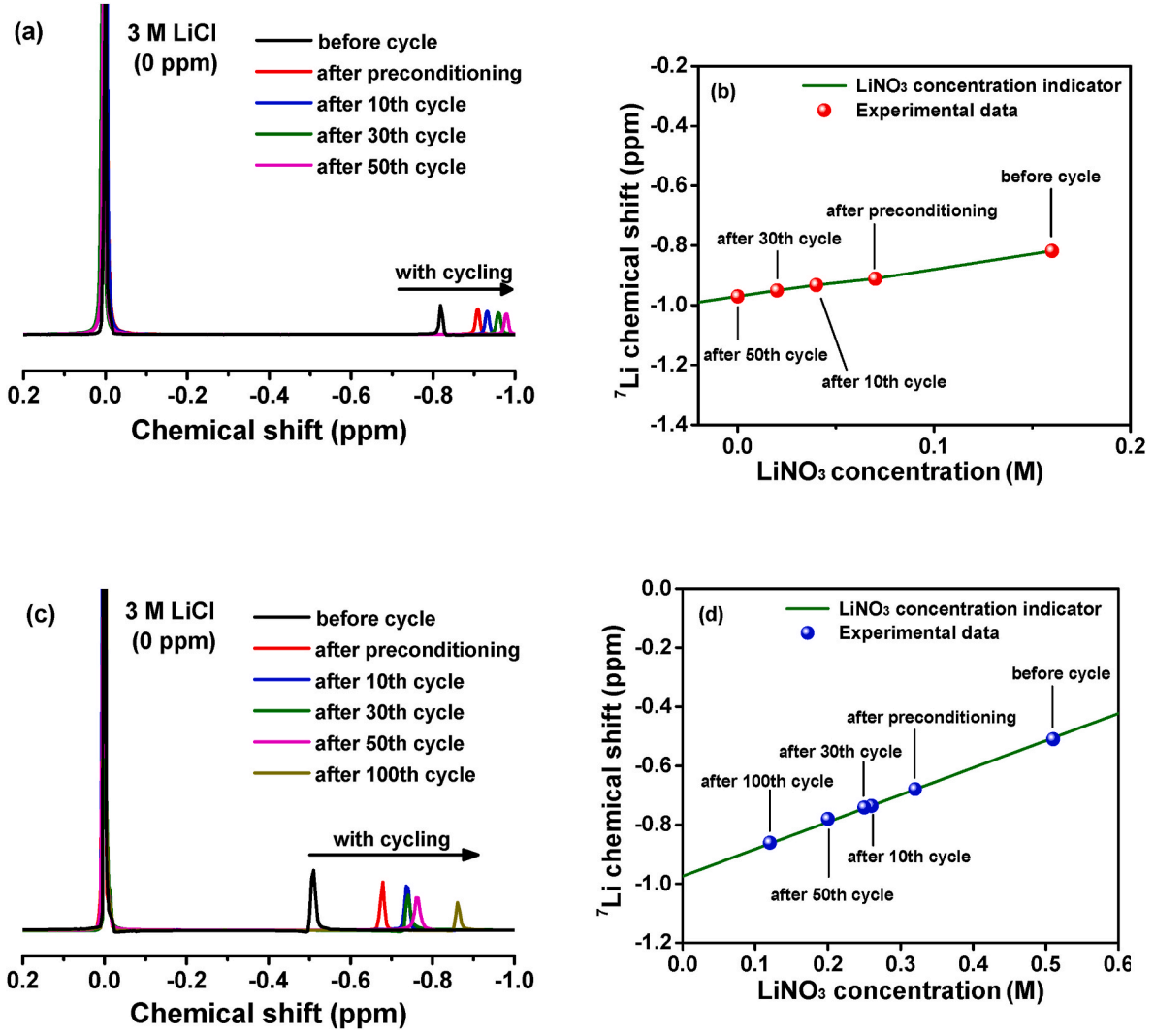


**Fig. 6.** $^7$Li NMR spectra of the electrolytes collected from the anode-free cells (a) without and (c) with LNR as functions of cycle number. Variations in the $LiNO_3$ concentrations of in the anode-free cells (b) without and (d) with LNR as a function of cycle number.

performance. We investigated the effect of $LiNO_3$ content in the LNR on the cycling performance. As presented in Fig. S12, an excessive amount of $LiNO_3$ resulted in low initial capacity and rapid capacity fading, while insufficient $LiNO_3$ showed a limited improvement in cycle life. Accordingly, the amount of $LiNO_3$ for maintaining stable cycling behavior was optimized to 0.68 mg $cm^{-2}$. Fig. 7a and b shows the voltage profiles of the Li (20 μm)/NCM cells without and with the LNR at 0.33 C and 25 °C, respectively, and their cycling performances are compared in Fig. 7c. The cell without the LNR exhibits good capacity retention until the 142nd cycle but subsequently shows rapid capacity fading, with a decrease in coulombic efficiency, finally leading to the cell failure. In contrast, the Li/NCM cell with the LNR exhibits quite stable cycling behavior, with a high capacity retention of 85.2 % after 300 cycles. Hence, the continuous release of $LiNO_3$ from the LNR enables the formation of a stable SEI layer on the Li metal anode, resulting in an improvement in the cycling stability of the Li/NCM cell. We calculated the energy densities of Li/NCM cells without and with LNR, as given in Table S2. Compared to the cell without LNR, the cell with LNR exhibited a 2.9 % reduction in gravimetric energy density and a 5.0 % loss in volumetric energy density. Although there is a slight loss in energy density, the Li/NCM cell with LNR exhibits a significant increase in cycle life. With respect to the compatibility with industrial calendaring process, the LNR layer prepared with electrospun PVdF-co-HFP exhibits excellent adhesion to the lithium electrode and superior flexibility, making it well-suited for industrial calendaring processes. Our results demonstrate the potential of the LNR system for use in enhancing the cycling performance of high-energy-density anode-free or Li metal batteries.

## 4. Conclusions

In this study, we prepared an additive reservoir system to store and continuously release $LiNO_3$ using an electrospun PVDF-*co*-HFP membrane as the framework. Based on XPS and NMR spectroscopy, the continuous release of $LiNO_3$ from the LNR delayed its depletion within the electrolyte. This resulted in the formation of an inorganic-rich, stable SEI layer that suppressed the dendritic growth of Li and undesirable side reactions with the liquid electrolyte. As a result, the anode-free and Li (20 μm)/$LiNi_{0.8}Mn_{0.1}Co_{0.1}O_2$ cells with the LNR exhibited superior cycling stabilities compared to those of the cells without the LNR. Hence, an additive reservoir system with the capacity to store and release $LiNO_3$, which is hardly soluble in the electrolyte, can effectively improve the cycle life of high-energy-density anode-free and Li metal batteries.

## CRediT authorship contribution statement

**Myung-Keun Oh:** Methodology, Investigation, Formal analysis, Data curation, Conceptualization. **Ji-Wan Kim:** Validation, Methodology, Investigation, Formal analysis. **Hee-Su Kim:** Methodology, Investigation, Formal analysis, Data curation. **Dong-Won Kim:** Writing – review & editing, Supervision, Project administration.

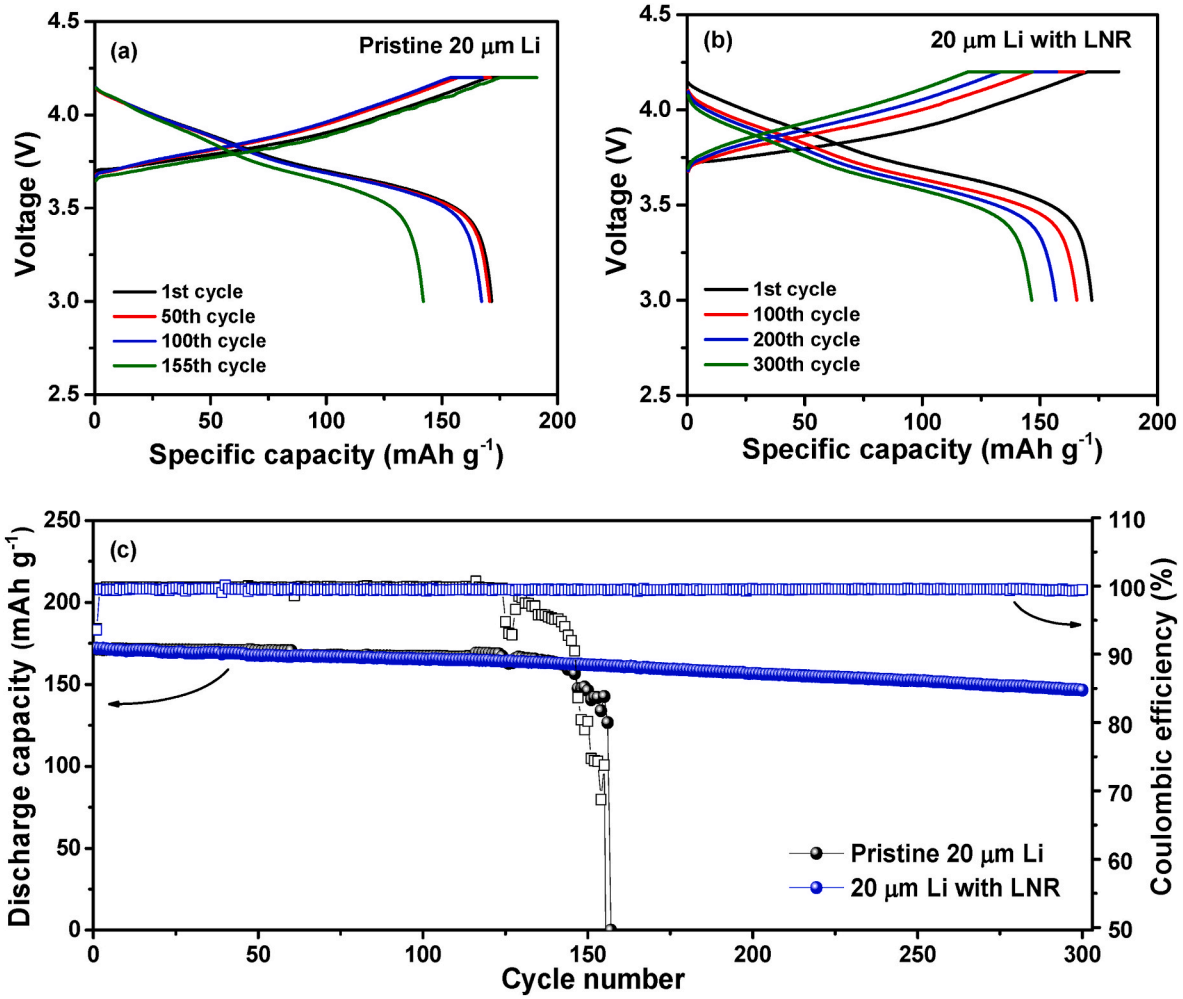


**Fig. 7.** Voltage profiles of the Li/NCM cells (a) without and (b) with the LNR. (c) Cycling performance of the Li/NCM cells at 0.33 C and 25 °C.

## Declaration of competing interest

The authors declare that they have no known competing financial interests or personal relationships that could have appeared to influence the work reported in this paper.

## Acknowledgements

This work was supported by the Hyundai Motor Company and the National Research Foundation of Korea (NRF) grant funded by the Korea government (MSIT) (RS-2024-00454354).

## Appendix A. Supplementary data

Supplementary data to this article can be found online at https://doi.org/10.1016/j.jpowsour.2025.237011.

## Data availability

Data will be made available on request.

## References

[1] Z.P. Cano, D. Banham, S. Ye, A. Hintennach, J. Lu, M. Fowler, Z. Chen, Batteries and fuel cells for emerging electric vehicle markets, Nat. Energy 3 (2018) 279–289, https://doi.org/10.1038/s41560-018-0108-1.
[2] J. Liu, Z. Bao, Y. Cui, E.J. Dufek, J.B. Goodenough, P. Khalifah, Q. Li, B.Y. Liaw, P. Liu, A. Manthiram, Y.S. Meng, V.R. Subramanian, M.F. Toney, V. V. Viswanathan, M.S. Whittingham, J. Xiao, W. Xu, J. Yang, X.Q. Yang, J.G. Zhang, Pathways for practical high-energy long-cycling lithium metal batteries, Nat. Energy 4 (2019) 180–186, https://doi.org/10.1038/s41560-019-0338-x.
[3] W. Xu, J.L. Wang, F. Ding, X.L. Chen, E. Nasybutin, Y.H. Zhang, J.-G. Zhang, Lithium metal anodes for rechargeable batteries, Energy Environ. Sci. 7 (2014) 513–537, https://doi.org/10.1039/c3ee40795k.
[4] P. Albertus, S. Babinec, S. Litzelman, A. Newman, Status and challenges in enabling the lithium metal electrode for high-energy and low-cost rechargeable batteries, Nat. Energy 3 (2018) 16–21, https://doi.org/10.1038/s41560-017-0047-2.
[5] B. Liu, J.-G. Zhang, W. Xu, Advancing lithium metal batteries, Joule 2 (2018) 833–845, https://doi.org/10.1016/j.joule.2018.03.008.
[6] L. Su, H. Charalambous, Z. Cui, A. Manthiram, High-efficiency, anode-free lithium–metal batteries with a close-packed homogeneous lithium morphology, Energy Environ. Sci. 15 (2022) 843, https://doi.org/10.1039/d1ee03103a.
[7] X. Zhang, L. Huang, B. Xie, S. Zhang, Z. Jiang, G. Xu, J. Li, G. Cui, Deciphering the thermal failure mechanism of anode-free lithium metal pouch batteries, Adv. Energy Mater. 13 (2023) 202203648, https://doi.org/10.1002/aenm.202203648.
[8] C. Fang, J. Li, M. Zhang, Y. Zhang, F. Yang, J.Z. Lee, M. Lee, J. Alvarado, M. A. Schroeder, Y. Yang, B. Lu, N. Williams, M. Ceja, L. Yang, M. Cai, J. Gu, K. Xu, X. Wang, Y.S. Meng, Quantifying inactive lithium in lithium metal batteries, Nature 572 (2019) 511–515, https://doi.org/10.1038/s41586-019-1481-z.
[9] J. Pokharel, A. Cresce, B. Pant, M. Yang, A. Gurung, W. He, A. Baniya, B. Lamsal, Z. Yang, S. Gent, X. Xian, Y. Cao, W.A. Goddard, K. Xu, Y. Zhou, Manipulating the diffusion energy barrier at the lithium metal electrolyte interface for dendrite-free long-life batteries, Nature 15 (2024) 3085, https://doi.org/10.1038/s41467-024-47521-z.
[10] X. Wang, S. Li, W. Zhang, D. Wang, Z. Shen, J. Zheng, H.-L. Zhuang, Y. He, Y. Lu, Dual-salt-additive electrolyte enables high-voltage lithium metal full batteries capable of fast-charging ability, Nano Energy 289 (2021) 106353, https://doi.org/10.1016/j.nanoen.2021.106353.
[11] Y. Liu, Y. Xu, Porous membrane host-derived in-situ polymer electrolytes with double-stabilized electrode interface enable long cycling lithium metal batteries, Chem. Eng. J. 433 (2022) 134471, https://doi.org/10.1016/j.cej.2021.134471.
[12] Q. Ran, J. Liu, L. Li, Q. Hu, F. Nie, H. Zhao, X. Liu, Crystallographic oriented plating by using lithiophilic ionic additives in carbonate electrolyte for enabling high voltage lithium metal batteries, Chem. Eng. J. 465 (2023) 142937, https://doi.org/10.1016/j.cej.2023.142937.
[13] Q. Wang, Y. Ma, Y. Wang, X. He, D. Zhang, Z. Li, H. Sun, Q. Sun, B. Wang, L.Z. Fan, In situ catalytic polymerization of $LiNO_3$-containing PDOL electrolytes for high-energy quasi-solid-state lithium metal batteries, Chem. Eng. J. 484 (2024) 149757, https://doi.org/10.1016/j.cej.2024.149757.
[14] J.-W. Kim, M.-K. Oh, Y.-A. Kim, U.T. Nakate, E.-J. Kwon, S. Seo, W.-K. Kim, K.-H. Ryu, D.-W. Kim, Enhanced cycle life of lithium metal batteries via modulating the lithium-ion solvation sheath with a cross-linked gel polymer electrolyte, J. Power Sources 598 (2024) 234183, https://doi.org/10.1016/j.jpowsour.2024.234183.
[15] A. Wang, Y. Nie, Y. Zhao, D. Xu, L. Zhang, Z. Zhao, L. Ren, S. Zhou, X. Liu, J. Luo, Functional copolymer derived self-adapting LiF-rich interphase toward deep cycling lithium metal batteries, Adv. Funct. Mater. 34 (2024) 2401462, https://doi.org/10.1002/adfm.202401462.
[16] X.-Q. Zhang, X. Chen, L.-P. Hou, B.-Q. Li, X.-B. Cheng, J.Q. Huang, Q. Zhang, Regulating anions in the solvation sheath of lithium ions for stable lithium metal batteries, ACS Energy Lett. 4 (2019) 411–416, https://doi.org/10.1021/acsenergylett.8b02376.
[17] X. Xu, X. Yue, Y. Chen, Z. Liang, Li plating regulation on fast-charging graphite anodes by a triglyme-$LiNO_3$ synergistic electrolyte additive, Angew. Chem. 62 (2023) e2023069, https://doi.org/10.1002/anie.202306963.
[18] C. Yan, Y. Yao, X. Chen, X. Cheng, X. Zhang, J. Huang, Q. Zhang, Lithium nitrate solvation chemistry in carbonate electrolyte sustains high-voltage lithium metal batteries, Angew. Chem. 57 (2018) 4055–4059, https://doi.org/10.1002/anie.201807034.
[19] Q. Liu, Y. Xu, J. Wang, B. Zhao, Z. Li, H. Wu, Sustained release nanocapsules enable long lasting stabilization of li anode for practical li metal batteries, Nano-Micro Lett. 12 (2020) 176, https://doi.org/10.1007/s40820-020-00514-1.
[20] J.-T. Kim, I. Phiri, S.-Y. Ryou, Incorporation of embedded protective layers to circumvent the low $LiNO_3$ solubility problem and enhance li metal anode cycling performance, ACS Appl. Energy Mater. 6 (2023) 2311–2319. https://pubs.acs.org/doi/10.1021/acsaem.2c03511.
[21] D. Jin, Y. Roh, T. Jo, M.-H. Ryou, H. Lee, Y.M. Lee, Robust cycling of ultrathin li metal enabled by nitrate-preplanted li powder composite, Adv. Energy Mater. 11 (2021) 2003769, https://doi.org/10.1002/aenm.202003769.
[22] Y. Xia, Y.F. Liang, D. Xie, X.L. Wang, S.Z. Zhang, X.H. Xia, C.D. Gu, J.P. Tu, A poly (vinylidene fluoride-hexafluoropropylene) based three-dimensional network gel polymer electrolyte for solid-state lithium-sulfur batteries, Chem. Eng. J 358 (2019) 1047–1053, https://doi.org/10.1016/j.cej.2018.10.092.
[23] T. Li, Y. Li, Y. Sun, Z. Qian, R. Wang, New insights on the good compatibility of ether-based localized high-concentration electrolyte with lithium metal, ACS Mater. Lett. 3 (2021) 838–844. https://pubs.acs.org/doi/10.1021/acsmaterialslett.1c00276.
[24] S. Chen, J. Zheng, D. Mei, K.-S. Han, M.-H. Engelhard, W. Zhao, W. Xu, J. Liu, J.-G. Zhang, High-voltage lithium-metal batteries enabled by localized high-concentration electrolytes, Adv. Mater. 30 (2018) 1706102, https://doi.org/10.1002/adma.201706102.
[25] D. Liu, X. Xiong, Q. Liang, X. Wu, H. Fu, An inorganic-rich SEI induced by $LiNO_3$ additive for a stable lithium metal anode in carbonate electrolyte, Chem. Commun. 57 (2021) 9232–9235, https://doi.org/10.1039/d1cc03676a.
[26] H. Chen, K. Chen, L. Luo, X. Liu, Z. Wang, A. Zhao, H. Li, X. Ai, Y. Fang, Y. Cao, $LiNO_3$-based electrolytes via electron-donation modulation for sustainable nonaqueous lithium rechargeable batteries, Angew. Chem. 63 (2024) e202316966, https://doi.org/10.1002/anie.202316966.
[27] J. Fu, X. Ji, J. Chen, L. Chen, X. Fan, D. Mu, C. Wang, Lithium nitrate regulated sulfone electrolytes for lithium metal batteries, Angew. Chem. 132 (2020) 22378–22385, https://doi.org/10.1002/ange.202009575.
[28] B. Xia, Y. Yang, J. Zhou, G. Chen, Y. Liu, H. Wang, M. Wang, Y. Lai, Using self-organizing maps to achieve lithium-ion battery cells multi-parameter sorting based on principle components analysis, Energies 12 (2019) 1980, https://doi.org/10.3390/en12152980.
[29] T. Ono, K. Shimoda, M. Tsubota, S. Kohara, T. Ichikawa, K.-I. Kojima, M. Tansho, T. Shimizu, Y. Kojima, Ammonia desorption property and structural changes of $LiAl(NH_2)_4$ on thermal decomposition, J. Phys. Chem. C 115 (2011) 10284–10291, https://doi.org/10.1021/jp111656v.
[30] J. Qian, B.D. Adams, J. Zheng, W. Xu, W.A. Henderson, J. Wang, M.E. Bowden, S. Xu, J. Hu, J. Zhang, Anode-free rechargeable lithium metal batteries, Adv. Funct. Mater. 26 (2016) 7094–7102, https://doi.org/10.1002/adfm.201602353.
[31] C. Wan, S. Xu, M.Y. Hu, R. Cao, J. Qian, Z. Qin, J. Liu, K.T. Mueller, J. Zhang, J. Hu, Multinuclear NMR study of the solid electrolyte interface formed in lithium metal batteries, ACS Appl. Mater. Interfaces 9 (2017) 14741–14748, https://doi.org/10.1021/acsami.6b15383.
[32] L.D. Ellis, I.G. Hill, K.L. Gering, J.R. Dahn, Synergistic effect of $LiPF_6$ and $LiBF_4$ as electrolyte salts in lithium-ion cells, J. Electrochem. Soc. 164 (2017) A2426, https://doi.org/10.1149/2.0811712jes.
[33] J. Li, W. Li, Y. You, A. Manthiram, Extending the service life of high-Ni layered oxides by tuning the electrode-electrolyte interphase, Adv. Energy Mater. 8 (2018) 1801957, https://doi.org/10.1002/aenm.201801957.
[34] Z. Liang, C. Li, D. Zuo, L. Zeng, T. Ling, J. Han, J. Wan, Achieving stable Zn metal anode through novel interface design with multifunctional electrolyte additive, Energy Storage Mater. 63 (2023) 102980, https://doi.org/10.1016/j.ensm.2023.102980.
[35] X. Chena, X. Wang, D. Fang, A review on C1s XPS-Spectra for some kinds of carbon materials, fuller. Nanotub, Carbon Nanostructures 28 (2020) 1048–1058, https://doi.org/10.1080/1536383X.2020.1794851.
[36] A.-H. Ban, S.-J. Pyo, W.J. Bae, H.-S. Woo, J. Moon, D.-W. Kim, Dual-type gel polymer electrolyte for high-voltage lithium metal batteries with excellent cycle life, Chem. Eng. J. 475 (2023) 146266, https://doi.org/10.1016/j.cej.2023.146266.
[37] V. Sharova, A. Moretti, T. Diemant, A. Varzi, R. Behm, S. Passerini, Comparative study of imide-based li salts as electrolyte additives for Li-ion batteries, J. Power Sources 31 (2018) 43–52, https://doi.org/10.1016/j.jpowsour.2017.11.045.
[38] H. Jin, H. Liu, H. Cheng, P. Zhang, M. Wang, The synergistic effect of lithium bis (fluorosulfonyl)imide and lithium nitrate for high-performance lithium metal anode, J. Electroanal. Chem. 874 (2020) 114484, https://doi.org/10.1016/j.jelechem.2020.114484.
[39] L. Yoshida, Y. Matsui, M. Deguchi, T. Hakari, M. Watanabe, M. Ishikawa, Improvement of lithium-sulfur battery performance by porous carbon selection and LiFSI/DME electrolyte optimization, ACS Appl. Mater. Interfaces 15 (2023) 37467–37476, https://doi.org/10.1021/acsami.3c06624.

[40] J. Zhang, H. Zhang, R. Li, D. Lu, S. Zhang, X. Xiao, S. Geng, F. Wang, T. Deng, L. Chen, X. Fan, Diluent decomposition-assisted formation of LiF-rich solid-electrolyte interfaces enables high-energy Li-metal batteries, J. Energy Chem. 598 (2024) 234183, https://doi.org/10.1016/j.jechem.2022.11.013.

[41] C. Zhang, Q. Lan, Y. Liu, J. Wu, H. Shao, H. Zhan, Y. Yang, A dual-layered artificial solid electrolyte interphase formed by controlled electrochemical reduction of LiTFSI/DME-LiNO3 for dendrite-free lithium metal anode, Electrochim. Acta 306 (2019) 407–419, https://doi.org/10.1016/j.electacta.2019.03.162.

[42] Y. Zhao, T. Zhou, L. Jeurgens, X. Kong, J. Choi, A. Coskun, Electrolyte engineering for highly inorganic solid electrolyte interphase in high performance lithium metal batteries, Chem 9 (2023) 682–697, https://doi.org/10.1016/j.chempr.2022.12.005.

[43] Q. Wang, C. Zhao, Z. Yao, J. Wang, F. Wu, S. Kumar, S. Ganapathy, S. Eustace, X. Bai, B. Li, J. Lu, M. Wagemaker, Entropy-driven liquid electrolytes for lithium batteries, Adv. Mater. 35 (2023) 2210677, https://doi.org/10.1002/adma.202210677.

[44] J. Zhong, Z. Wang, X. Yi, X. Li, H. Guo, W. Peng, J. Wang, G. Yan, Breaking the solubility limit of LiNO3 in carbonate electrolyte assisted by BF3 to construct a stable SEI film for dendrite-free lithium metal batteries, Small 20 (2024) 2308678, https://doi.org/10.1002/smll.202308678.

[45] M. Schmeisser, P. Illner, R. Puchta, A. Zahl, R. Eldik, Gutmann donor and acceptor numbers for ionic liquids, Chem. Eur J. 18 (2012) 10969–10982, https://doi.org/10.1002/chem.201200584.